SUPPLEMENTARY INFORMATION

The dynamics of scattering in undulatory active collisions

Jennifer M. Rieser, Perrin E. Schiebel, Arman Pazouki, Feifei Qian, Zachary Goddard, Kurt Wiesenfeld, Andrew Zangwill, Dan Negrut, Daniel I. Goldman

1. Experiment

Our 13-segment-robotic snake, shown in Fig. 1a, had 12 Dynamixel AX-12A servo motors connected together with custom-designed 3D-printed plastic brackets, and a Robotis CM-700 controller was programmed to command the angular position of each motor to vary sinusoidally with time and position along the body. Robot segments were 3.7 cm wide, and 3-cm tall all interior segments were 5.1 cm long. The head, 6.0 cm long, added a nearly-spherical nose cap to the interior segment design, and the tail, 7.5 cm long, was adapted to have a cylindrical cap. The robot mass was 1.13 kg and the fully-extended length was around 80 cm.

The snake moved in a model heterogeneous terrain, created from a level wooden platform (dimensions 2.4 m wide x 3.6 m long) covered by a firm rubber mat. Obstacles consisted of a single row of vertical polycarbonate posts (radius, $r = 0.023$ m) anchored to the platform (see Fig. 2). Before each experiment, the robot motor configuration was reset and the robot was manually positioned and oriented so the initial heading was transverse to the post row. Positions of infrared-reflective markers atop each robot segment were identified and recorded at 120 Hz by four Optitrack Flex13 infrared cameras (positions were accurate to within 0.1 mm). Using the tracking data, we quantified the final heading of the robot, θ (see Fig. 2b-c), for each trajectory by identifying and fitting lines to the extrema of segment trajectories (for at least three undulations) after the tail had moved beyond the post row.

2. Wheel friction

To characterize the robot-substrate interaction forces during movement, we designed a custom, 3D printed bracket to attach a single pair of Lego wheels to a 6-axis force-torque transducer (Nano 43, ATI Industrial Automation, Apex, NC, USA) and mounted the force sensor to a 6-axis industrial robot arm (Denso VS087A2-AV6-NNN-NNN). The robot arm was programmed to repeatedly execute the following automated procedure: (1) rotate the wheels by a specified angle, ψ, relative to the dragging direction and begin recording forces at 1 kH; (2) lower the wheels to a predetermined height, H, at which point wheel contact with the substrate (ethylene-vinyl acetate (EVA) Soft Linking Mats) had been established and the normal load on the wheels was comparable to the weight of a robot segment; (3) horizontally translate the wheels 40 cm across the substrate at a constant speed, $v = 10$ mm/s; (4) raise the wheels, stop recording forces, and return to the initial position.

Five trials were performed per ψ, which was varied from 0° to 90° (parallel to perpendicular to the wheel axle) in increments of one degree. For each trial, forces were decomposed into components along the wheel axle, $F_\perp$, and along the preferred rolling direction, $F_\parallel$. Force components quickly reached and subsequently maintained a near-constant value for most of the dragging distance, therefore, we estimated the steady-state values by averaging each component over the five trials within this near-constant window. Functions were fit to $F_\perp$ and $F_\parallel$ (shown as the curves in Fig. 1d) these forces could be incorporated into the Chrono simulation. Numerical values of fit parameters along with corresponding 95% confidence intervals are given in Table S1.

$$F_\perp(\psi) = a\psi + \frac{b}{1 + e^{-\psi/c}} + d$$

$$F_\parallel(\psi) = p_1\psi^4 + p_2\psi^3 + p_3\psi^2 + p_4\psi + p_5$$

3. Simulation

The simulation-based studies conducted relied on an open-source simulation framework called Chrono [1]. For a constrained multibody dynamics problem, Chrono formulates a set of index three differential-algebraic equations whose solution captures the time evolution of the dynamic system. All simulation results reported here were obtained

TABLE S1. fit parameter values and 95% confidence intervals for $F_{\parallel}$ and $F_{\perp}$.

parameter	value	95% confidence interval
a	0.0011	$(0.0010, 0.0012)$
b	0.47	$(0.42, 0.51)$
c	1.1	$(0.98, 1.21)$
d	-0.19	$(-0.24, -0.15)$
p_1	-7.8×10^{-9}	$(-1.2 \times 10^{-8}, -3.1 \times 10^{-9})$
p_2	1.2×10^{-6}	$(2.9 \times 10^{-7}, 2.1 \times 10^{-6})$
p_3	-8.7×10^{-5}	$(-1.4 \times 10^{-4}, -3.2 \times 10^{-5})$
p_4	0.0030	$(0.0018, 0.0043)$
p_5	0.097	$(0.089, 0.110)$

TABLE S2. Attributes of the snake and posts in the simulation.

Snake geometry	Segment length	5.1 cm
	Segment height	3.5 cm
	Segment width	3.2 cm
	Head radius	1.92 cm
	Tail radius	1.8 cm
	Tail height	3.5 cm
	Joint radius	1.85 cm
	Density	1.2 g/cm^3
Snake motion	Wave amplitude (ζ_{max})	0.605 rad
	Wave frequency (f)	0.15 Hz
post	Radius	2.25 cm
	Height	20 cm
	Density	1.2 g/cm^3

using a half implicit, first order, symplectic Euler time integration method and a successive over-relaxation iteration scheme. Geometric overlaps between contacting objects was used to approximate local deformations at contact points. The contact force between mating surfaces was calculated via a Hertzian contact force model [2],

$$F_n = k_n \delta_n - g_n v_n^r$$

$$F_t = k_t \delta_t,$$

where the subscripts n and t denote the contact force components, F_n and F_t, in the normal and tangential directions, respectively, δ_n is the overlap of two interacting bodies, v_n^r is the relative velocity of the bodies at the contact point, δ_t is a relative displacement in the tangential direction at the contact point, and the friction force is capped as $F_t \leq \mu F_n$ (for more detail, see [3]). For the contact of parallel cylinders, $k_n = \pi/4Y^*l$ is the contact stiffness modulus and $k_t = 2k_n/7$. Here l is the cylinder length, i.e. the height of a segment, and Y^* is the effective Young's modulus, defined based on Young's modulus, Y, and Poisson's ratio, ν, of the mating surfaces as

$$1/Y^* = (1 - \nu_1^2)/Y_1 + (1 - \nu_2^2)/Y_2.$$

Contact forces between a post and a segment with a flat surface were calculated in a similar fashion. To allow for larger integration time-steps and thus reduce simulation time, the value of Young's modulus was chosen to be smaller than the actual one. Drawing on a sensitivity analysis that quantified the impact of relaxing Y on the accuracy of the simulation results, we used $Y = 2.5 \times 10^6$ and $\nu = 0.4$. The damping coefficient, g_n, depends on the material coefficient of restitution and collision scenario [4]. We used a larger value, g_n ($\sim 10^3$), to enforce a plastic contact.

The geometry of the snake model was modeled through a set of shape primitives such as box and cylinders. The body components were connected by revolute joints, which removed five out of six relative degrees of freedom. Additional light-weight cylinders were positioned on the joints to facilitate, from a geometric perspective, a smooth interaction of the segments with the cylindrical posts. Table S2 shows parameter values used.

Simulations were then validated by comparing experimental and simulated trajectories and forces for snake interacting with a single post. In experiments, forces exerted by the robot during collisions with the post were recorded by mounting the post to an ATI Nano 43 6-axis force-torque transducer. Forces exerted by the robot onto the posts for the trials shown in Fig. 2 are shown in Fig. S1a (single post) and Fig. S1b (multi-post). This comparison is representative of agreement between simulation and experiment: trajectories for similar collision states produced nearly-identical trajectories and forces were often comparable and exhibited similar structure in both simulation and experiment. While there were some quantitative differences between simulation and experimental forces, these discrepancies did not seem to affect the kinematic agreement. A time step convergence analysis revealed that forces and resulting trajectories were insensitive to the time step, Δt, for $\Delta t < 6 \times 10^{-4}$ s. $\Delta t = 10^{-4}$ s was selected for all the simulations presented here.

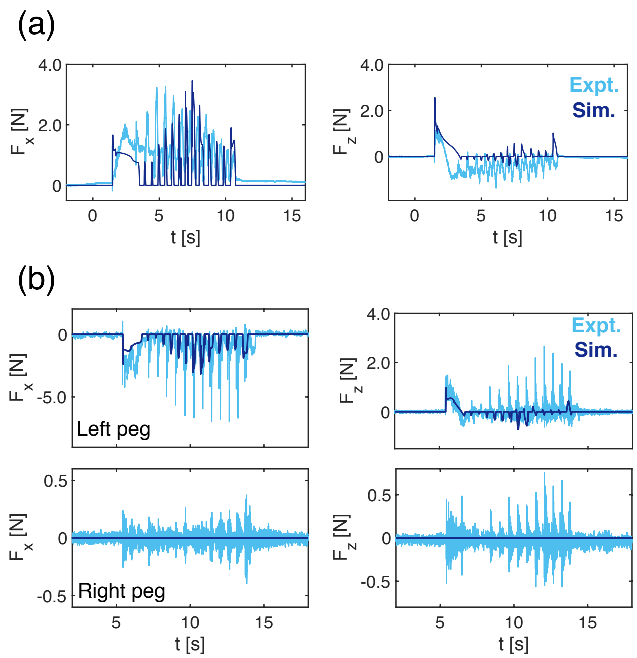

FIG. S1. **Experimental and simulation forces on posts.** (a) Forces exerted onto the post by the robot during the trajectory shown in Fig. 2b. (b) Forces exerted onto the posts by the robot during the trajectory shown in Fig. 2c.

In the multi-post simulations, the accuracy of the results improved significantly when, to mirror the presence of the revolute joints in the physical prototype, the snake model was augmented with spheres connecting the boxes used for the snake segments. The diameter of the connecting spheres was identical to the width of the robotic snake. The width of the cubic segments in the simulation was slightly reduced from that of the robotic snake to bury the edges inside the spherical joints and prevent the edge contact, particularly at large time step. Table S2 summarizes the attributes of the snake and the posts for simulations presented here.

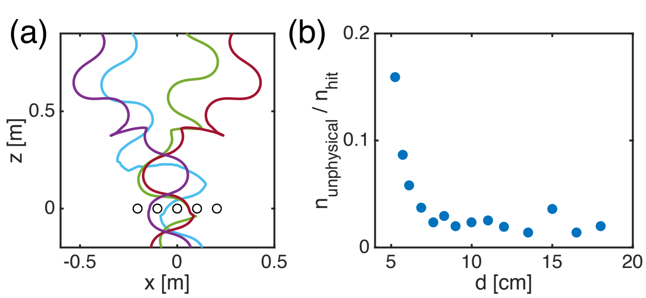

FIG. S2. **Unphysical simulation trajectories.** (a) Four examples of unphysical trajectories for $d = 5.7$ cm. The robot becomes pinned after the head has cleared the posts, and as a result, the body is rapidly reoriented. These situations do not occur in the experiment. (b) Fraction of simulations for each spacing that are unphysical.

At least $1,000$ simulations were run for each post configuration, and for each configuration, there were a few trajectories which were not physical. These typically occurred when the tail of the snake became stuck on the post, causing the entire snake to rapidly change direction. Four representative examples are shown in Fig. S2a. These were identified and removed from further analysis using the following criteria: if, at any point after the head has moved beyond the post row, (1) velocity of head is at least twice as large as maximum head velocity for the freely-moving snake, $v_{head} \geq 2v_{max,free}$ and (2) force on the head does not exceed a nominal value, chosen here to be $F_{head} \leq 0.01$ N. Fig. S2b shows (for $\zeta_{max} = 0.605$ rad), as a function of post spacing, how many unphysical trajectories occurred relative to the number of simulations that had collisions with the posts.

4. Small and large ζ_{max}: Qualitatively different spacing dependence

We find that the distribution dependence on spacing presented in Fig. 10 does not hold for all ζ_{max} angular amplitudes of oscillation. If ζ_{max} is sufficiently small, the distance swept out in a single cycle, $2\ell\zeta_{max}$ does not exceed the post diameter, $2r$. The qualitative behavior change we observe for small ζ_{max} is consistent with this observation, falling to the left of the dashed line in Fig. 10c. For large ζ_{max}, the body becomes very curved and points along the body in the direction of travel are no longer monotonically increasing from tail to head. We suspect that this may set a qualitative change in behavior as well. Fig. S3 shows the dependence of the spread of the distributions, θ_{70}, on the inter-post spacing, d, for two amplitudes with qualitatively different behavior.

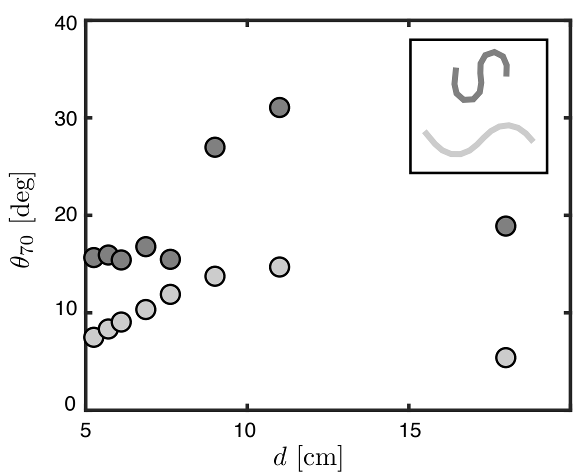

FIG. S3. **Scattering angle distribution dependence on spacing for large and small angular amplitude.** When ζ_{max} is outside of the range presented in the main text, the qualitative dependence of θ_{70} on d changes. The light gray points show this dependence for small ζ_{max}, and the dark gray points show the dependence for large ζ_{max}

5. Multi-post configuration: One dominant head collision

To demonstrate that there is one dominant collision in the multi-post configuration, we first show that most simulations, even for small spacings, had one head-post collision. Fig. S4a shows how many of the simulations, n_{hit}, had at least one collision between the head of the snake and the post row relative to the total number of simulations, n_{sim}. The number of simulations in which two or more collisions occurred, n_{2+}, compared to n_{hit} is shown in Fig. S4b.

Of the simulations in which multiple collisions occur, we next show that the second-longest collision is typically not of comparable duration. In Fig. S4c, two-dimensional probability densities of second-longest vs longest duration are shown for four post configurations. If collisions were of comparable durations, the density of points would lie along the black lines in each plot. However, in each case, most of the points are concentrated below the line. This, along with the decreasing number of simulations for which multiple collisions occur, confirms that there is typically one dominant collision.

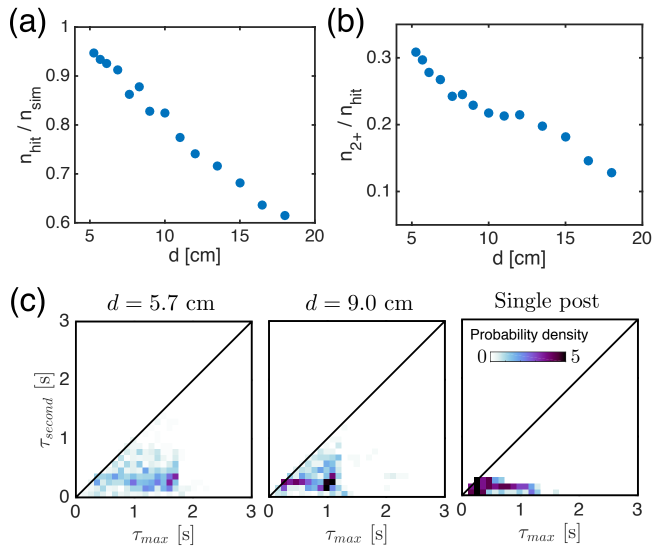

FIG. S4. **Fraction of simulations with head collisions.** (a) Fraction of simulations for which at least one head-post collision occurred as a function of spacing. (b) Fraction of simulations in (a) for which two or more collisions occurred. (c) Probability maps for second-longest vs longest durations for $d = 5.7$ cm (left) to $d = 9.0$ cm (middle) to single post (right). Only simulations for which there were at least two collisions are shown here.

6. Single- and multi-post collision states

Fig. S5 shows how the density collision states depends on the inter-post spacing. For the single-post simulations (bottom right), all allowed states are evenly-sampled. As spacing is decreased, certain undulation-phase and impact location collision states become inaccessible, and others become more likely to occur. These excluded regions become larger as spacing becomes smaller, and the non-uniformity of the densities of remaining states becomes more pronounced.

For each post configuration, initial conditions within the relevant region were randomly generated. Therefore, we did not necessarily have information about precisely the same collision for single- and multi-post configurations. Therefore, to determine how collision states were influenced by the presence and location of additional posts, we identified, in (η, ϕ) space, the single-post state closest to each multi-post state by minimizing $\delta_{\eta\phi} = \sqrt{(\eta_s - \eta_m)^2 + (\phi_s - \phi_m)^2}$.

The distributions of distances between the single- and multi-post states are shown in the left column of Fig. S6. These distributions do not depend on post spacing, and in all cases, distances are typically small, so single-post points assigned to multi-post states are nearby in (η, ϕ) space. As a final check, we show in the right column of Fig. S6 that there is no significant correlation between $\delta_{\eta\phi}$ and deviation from the $\omega\tau_m = \omega\tau_s$ trend. Two-dimensional PDFs for two post configurations are shown, and the corresponding correlation coefficient for each spacing is given in each plot.

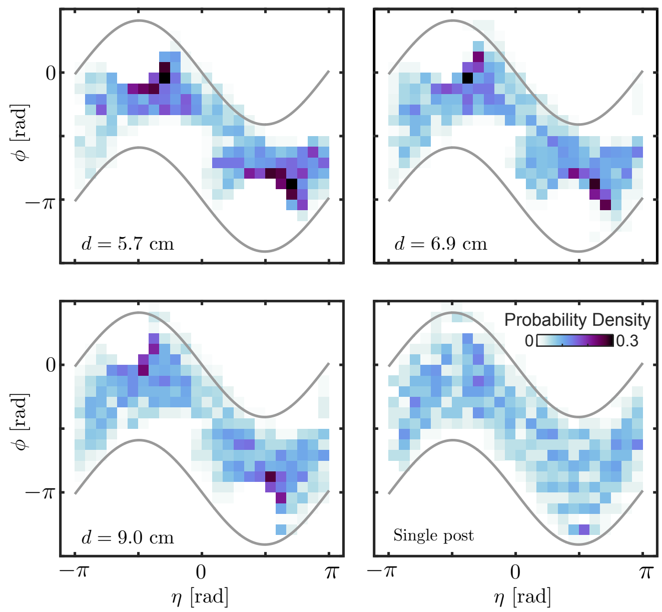

FIG. S5. **Densities of collision states.** Densities of states in the space of impact locations, ϕ, and wave phases, η. These states are shifted around as spacing is changed. In the single-post case, all allowed states are evenly sampled. As spacing is decreased when multiple posts are present, some regions become inaccessible and others more favored.

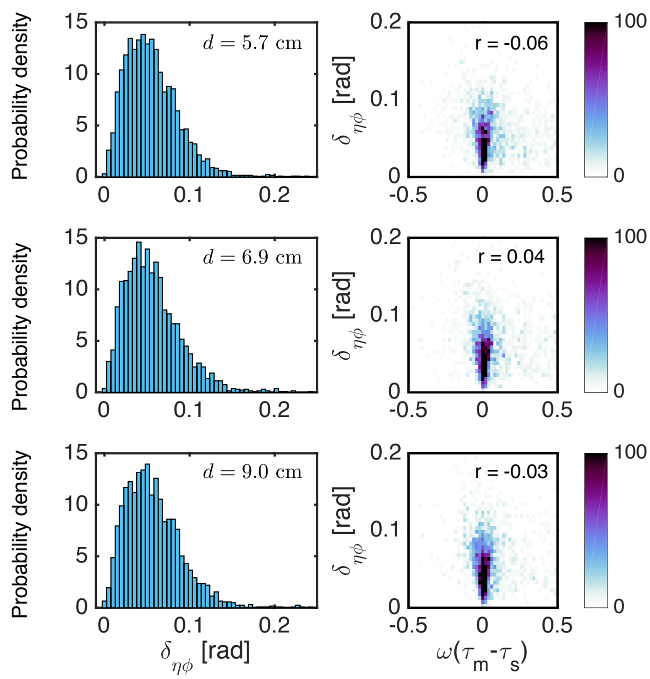

FIG. S6. **Distances between single- and multi-post states.** Each row shows data for a spacing specified in left plot. Left column: Probability distributions of distances between nearest single and multi-peg states (nearest is defined by the smallest euclidean distance between states in (η, ϕ)-space). Right column: Two dimensional PDFs showing that there is no significant correlation between deviation from $\omega\tau_m = \omega\tau_s$ line and distance between nearest single- and multi-peg collision states.

7. Supplementary movies

Movie 1. **Robotic snake in single-post environment.** A view of the robotic snake moving toward and interacting with a single post. The sliding/pushing head-post interaction is visible here.

Movie 2. **Robotic snake in multi-post environment.** An overhead view of several experiments in which the robotic snake moving toward, interacting with, and subsequently exiting the multi-post array (here, $d = 5.7$ cm). The final heading depends on the initial placement of robot, which is varied along the fore-aft direction here.

Movie 3. **Simulated snake in multi-post environment.** Three examples of the simulated snake interacting with a multi-post array ($d = 5.7$ cm).

Movie 4. **Emergence of preferred directions.** Summation of binary images created from the head trajectory of the robot in each of 329 experiments for $d = 5.7$ cm. Trajectories from different initial positions are added in a randomized order. As more experiments are included, a more complete picture of possible interactions and outcomes appears and preferred scattering directions emerge.

[1] A. Tasora, R. Serban, H. Mazhar, A. Pazouki, D. Melanz, J. Fleischmann, M. Taylor, H. Sugiyama, and D. Negrut, in *High Performance Computing in Science and Engineering Lecture Notes in Computer Science*, edited by T. Kozubek (Springer, 2016) pp. 19–49.

[2] K. L. Johnson, *Contact mechanics* (Cambridge University Press, 1987).

[3] J. Fleischmann, R. Serban, D. Negrut, and P. Jayakumar, Journal of Computational and Nonlinear Dynamics **11**, 044502 (2016).

[4] M. Machado, P. Moreira, P. Flores, and H. M. Lankarani, Mechanism and Machine Theory **53**, 99 (2012).